The Astrophysical Journal, 768:108 (7pp), 2013 May 10 doi:10.1088/0004-637X/768/2/108

THE GALACTIC CENTER CLOUD G2—A YOUNG LOW-MASS STAR WITH A STELLAR WIND

N. Scoville[1] and A. Burkert[2,3,4]
[1] California Institute of Technology, MC 249-17, 1200 East California Boulevard, Pasadena, CA 91125, USA
[2] University Observatory Munich, Scheinerstrasse 1, D-81679 Munich, Germany
[3] Max-Planck-Institute for Extraterrestrial Physics, Giessenbachstrasse 1, D-85758 Garching, Germany
Received 2013 February 10; accepted 2013 February 25; published 2013 April 19

ABSTRACT

We explore the possibility that the G2 gas cloud falling in toward SgrA* is the mass-loss envelope of a young T Tauri star. As the star plunges to smaller radius at 1000–6000 km s^{-1}, a strong bow shock forms where the stellar wind is impacted by the hot X-ray emitting gas in the vicinity of SgrA*. For a stellar mass-loss rate of $4 \times 10^{-8}\ M_\odot$ yr^{-1} and wind velocity 100 km s^{-1}, the bow shock will have an emission measure (EM $= n^2 vol$) at a distance $\sim 10^{16}$ cm, similar to that inferred from the IR emission lines. The ionization of the dense bow shock gas is potentially provided by collisional ionization at the shock front and cooling radiation (X-ray and UV) from the post shock gas. The former would predict a constant line flux as a function of distance from SgrA*, while the latter will have increasing emission at lesser distances. In this model, the star and its mass-loss wind should survive pericenter passage since the wind is likely launched at 0.2 AU and this is much less than the Roche radius at pericenter ($\sim$3 AU for a stellar mass of 2 $M_\odot$). In this model, the emission cloud will probably survive pericenter passage, discriminating this scenario from others.

Key words: accretion, accretion disks – black hole physics – Galaxy: center – ISM: clouds

Online-only material: color figures

1. INTRODUCTION

The recently discovered G2 cloud which is infalling toward SgrA* is a most intriguing astronomical discovery (Gillessen et al. 2012)—both its origin and nature are unclear as yet. Nevertheless, in the space of a few years from the first detection, one will observe its passage within $\sim$2200 Schwarzschild radii of the supermassive black hole—in 2013 September (Gillessen et al. 2013). Numerous observations, from radio to X-ray, are planned for this "once in an astronomical lifetime" event. At this point it is unclear if the cloud will survive pericenter passage and whether the activity of SgrA* will increase and over what timescale.

G2 was first observed in the H I Brγ and Brδ H I and 2.058 μm He I emission lines and detected in the near-infrared continuum with an extremely low 550 K color temperature (Gillessen et al. 2012; Eckart et al. 2013). Over the period 2004–2012 its three-dimensional (3D) velocity has increased from 1200 to over 2500 km s^{-1} (Gillessen et al. 2013). The latest orbital determination indicates an eccentricity of 0.966 and pericenter passage at 2×10^{15} cm from SgrA*, when the 3D velocity will be 6340 km s^{-1} (Gillessen et al. 2013). The orbital period is 198 yr with an apocenter distance of 1.6×10^{17} cm and velocity 108 km s^{-1}.

The observed flux in the Brγ line requires an ionized gas emission measure EM $= \int n_e^2 dvol \sim 10^{57}$ cm^{-3}. Surprisingly, the line flux exhibits no change greater than 10% over the 4 yr period (Gillessen et al. 2012, 2013). The cloud is resolved along its orbital path but unresolved in the transverse direction (i.e., $\leqslant 10^{15}$ cm); Gillessen et al. (2013) adopt an effective spherical radius 1.875×10^{15} cm for the emitting region and thereby deduce a mean density of 6×10^5 cm^{-3} and a total mass of $\sim 3\ M_{\rm earth}$ (assuming unity volume filling for the ionized gas). If this is the whole story (i.e., G2 has only the mass seen in the ionized gas and it is uniformly distributed), then it is clear that the cloud cannot survive pericenter passage since the Roche limit for tidal stability is $n \sim 1.5 \times 10^{17}$ cm^{-3}.

Several models have been proposed for the origin and nature of G2. Gillessen et al. (2012) and Burkert et al. (2012) have suggested that it may have formed as an interstellar cloud from colliding stellar winds in the young stellar ring at 2×10^{17} cm radius. Meyer & Meyer-Hofmeister (2012) suggest it is a ring of gas formed by a nova explosion. This might account for the low angular momentum and high eccentricity orbit. Burkert et al. (2012) model the subsequent hydrodynamic evolution of the cloud as it falls toward SgrA*—yielding reasonable agreement with the observed emissivities and kinematic evolution. Alternatively, Murray-Clay & Loeb (2012) proposed that G2 is a star with a protoplanetary disk, also scattered out of the young stellar ring (presumably from a triplet star system). Then as the system descends toward SgrA*, the disk is photoevaporated and tidally disrupted to produce the G2 cloud. With the orbital parameters known at the time they proposed this model, they argued that the outer protoplanetary disk at 5–10 AU would probably survive pericenter passage. However, with the most recent orbit determination (Gillessen et al. 2013), the disk will now probably be tidally stripped to within 2 AU radius at pericenter. In both of the above scenarios, it seems we are then extraordinarily fortunate to be observing a one-off event (i.e., a single orbital event) only noticed within a few years of its final demise. And yet there do not appear to be large numbers of similar objects farther out.

Here we explore a different scenario—G2 being a young low-mass T Tauri star, formed in the young stellar ring, and subsequently injected into the eccentric orbit. Many T Tauri stars have mass-loss winds at 200–500 km s^{-1} with $\dot{M} \sim$ 1–5 $\times 10^{-8}\ M_\odot$ yr^{-1} during their first million years. The mass-loss rates for those with measured rates ($\sim$50% of the sample) have a very large range of $10^{-6.5}$ to $10^{-10}\ M_\odot$ yr^{-1} (Hartigan et al. 1995) and a median value $2.5 \times 10^{-9}\ M_\odot$ yr^{-1}.

[4] Max-Planck-Fellow.

White & Hillenbrand (2004) obtained median values $10^{-7.0}$ and $10^{-8.2}\,M_\odot$ yr^{-1} for samples of 8 and 42 class I and II T Tauri stars, respectively. These outflows may originate as a centrifugally driven wind from the inner accretion disk (e.g., Blandford & Payne 1982). If so, then the observed velocities imply a launch radius well inside 1 AU radius from the star. This scenario for G2 has a superficial similarity to that of Murray-Clay & Loeb (2012) in having a young stellar object formed in the young stellar ring and having a circumstellar disk, but is very different in the physics of the mass-loss material and the possibility of pericenter survival. In the case of the T Tauri star wind, the outflow velocities $\sim$100 km s^{-1} are much larger than the 10 km s^{-1} expected for a photoevaporating disk with velocities $\sim$10 km s^{-1}. For the T Tauri star wind, a very dense bow shock is formed at radius $\sim 10^{14}$ cm and it is this gas which produces the observed emission lines. The stellar wind plus bow shock model readily reproduces the observed emission line fluxes using standard T Tauri star wind parameters.

In the following we analyze the mass-loss wind parameters and the interaction with the hot X-ray emitting gas in the vicinity of SgrA*, followed by a detailed numerical model for the bow shock at the upstream side of the plunging star. This allows us to track the evolution of the bow shock structures and their emissivity as a function of distance from SgrA*. Throughout most of the orbit, tidal stripping is not very significant since the bow shock on the front side of the star is pushed to smaller radii from the star as the orbit approaches the central black hole (due to the higher stellar velocity and higher density of the ambient hot X-ray gas at small galactic radii).

Using the derived density structure, we then analyze the ionization of the gas, concluding that the most likely source of the observed emission lines is the dense bow shock where the outflowing stellar wind meets the 10^8–10^9 K shocked layer of ambient gas. The ionization may be provided by photons in the free–free continuum and line emission of the gas cooling behind the shock. In addition, there will be collisional ionization as the wind material passes through the shock at 200–500 km s^{-1}. The expected Lyman continuum from young stars in the central parsec does not appear to be adequate. If the ionization is collisional it would account for the apparent constancy of the emission line fluxes, since the mass-loss rate is probably constant; however, unless the mass-loss rate is $>10^{-7}\,M_\odot$ yr^{-1} this ionization is insufficient to account for the inferred emission measures.

2. SPHERICAL MASS-LOSS WIND AND INTERACTION WITH CORONAL X-RAY EMITTING GAS

As the low-mass star with a stellar wind descends toward SgrA*, the outer envelope will interact with the ambient hot X-ray emitting gas (Baganoff et al. 2003; Muno et al. 2004; Shcherbakov & Baganoff 2010). For the stellar wind, we adopt the following fiducial numbers:

$$\dot{M} = 4 \times 10^{-8}\,M_\odot\ \mathrm{yr}^{-1} \equiv \dot{M}_* \tag{1}$$

and

$$V_W = 100\ \mathrm{km\ s}^{-1}, \tag{2}$$

which implies a density distribution in the mass envelope,

$$\rho_W = \frac{\dot{M}}{4\pi r^2 V_W} = 9.6 \times 10^{-17} \frac{\dot{M}_*}{r_{\mathrm{AU}}^2 V_{W\,100}}\ \mathrm{gr\ cm}^{-3} \tag{3}$$

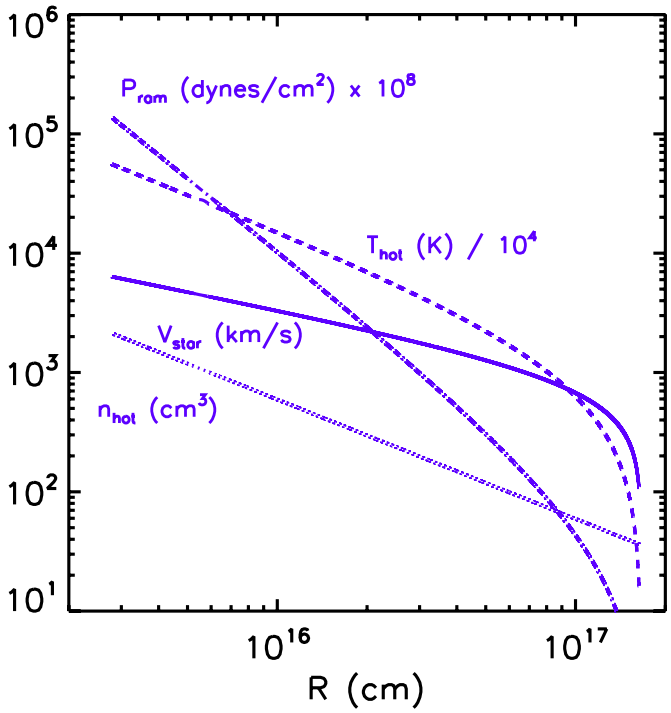

Figure 1. Stellar 3D velocity as a function of distance from SgrA*. The adopted density, temperature, and ram pressure of the hot X-ray emitting gas are also shown.

(A color version of this figure is available in the online journal.)

$$n_W \simeq 6 \times 10^7\ \mathrm{H\ cm}^{-3} \text{at 1 AU}. \tag{4}$$

For the stellar wind we adopt an inner launch radius which scales with the wind velocity, assuming the outflow velocity is equal to the escape velocity for material initially in circular orbit at the launch radius. This is a good approximation for outflow where the radial acceleration is gradual (rather than explosive).

For the hot ambient medium, we use the radial density and temperature distributions given by Burkert et al. (2012), which are similar but not identical to the X-ray model of Yuan et al. (2003). The temperature distribution was assumed appropriate to hydrostatic equilibrium of the gas in the potential of the $4.3 \times 10^6\,M_\odot$ SgrA* black hole. Specifically, we adopt:

$$\rho_{\mathrm{hot}} = 9.5 \times 10^{-22} \left(\frac{10^{16}\,\mathrm{cm}}{r}\right)\ \mathrm{gr\ cm}^{-3} \tag{5}$$

and

$$T_{\mathrm{hot}} = 2 \times 10^8 \left(\frac{10^{16}\,\mathrm{cm}}{r}\right) \mathrm{K}. \tag{6}$$

The above ignores the possibility that some of the X-ray emission is from stellar sources (Sazonov et al. 2012). These distributions are shown in Figure 1 together with the 3D stellar velocity and the resultant ram pressure from the hot X-ray emitting gas.

The outflowing stellar wind will terminate on the upstream side of the star in a shock front at the point where its ram pressure equals the thermal pressure of the hot ambient gas or the ram pressure of the hot gas. In the portion of the orbit where G2 is currently observed, it is plunging with velocity significantly greater than the local circular virial velocity; thus, the ram pressure is likely to dominate the hot gas thermal pressure (since the thermal temperature of this gas was estimated assuming

virial equilibrium in the central potential, which is dominated by the black hole at these radii).

The bow shock of the stellar wind against the hot medium will have a stagnation or standoff radius in front of the star (balancing ram pressures) at:

$$R_s^2 = \frac{\dot{M}_* V_W}{4\pi \rho_H V_*^2}, \quad (7)$$

where $\rho_H \sim 10^{-21}$ gr cm^{-3} is the mass density in the hot medium at an orbital distance of $\sim 10^{16}$ cm, corresponding to the position of G2 in mid 2012. For mid 2012, $V_* = 2000$ km s^{-1} and therefore

$$R_s = 2.3 \times 10^{14}\ \mathrm{cm} \left[\frac{\dot{M}_* V_{W\,100}}{\rho_{\mathrm{H}-21} V_{*2000}} \right]^{1/2} \sim 14\ \mathrm{AU}. \quad (8)$$

At this radius the wind density is $n_{W0} = 3 \times 10^5$ H cm^{-3}.

For the mass-loss star moving supersonically through the hot medium near SgrA*, the bow shock on the upstream side will occur at R_s and a conical compressed gas layer will extend downstream from the star. In fact there will be two shocked layers, the first where the ambient hot gas meets the stellar wind bow shock, and the second, an interior bow shock, where the outflowing stellar wind meets the compressed gas at the stagnation point on the upstream side of the star. We will refer to these as the *hot bow shock* and the *cold bow shock,* respectively (Figure 3).

The immediate post shock gas temperatures are given by $T = 1.38 \times 10^5 (V_{\mathrm{shock}}/100\ \mathrm{km\ s^{-1}})^2$ K for an ionized gas (McKee & Hollenbach 1980), implying temperatures of 10^8–10^9 and $\sim 5 \times 10^5$ K, respectively, behind the two bow shocks.

The first shock front will be adiabatic since this very hot gas cools slowly. The density in this shock is shown in Figure 4 and is ~ 1000 cm^{-3}. The second shock front has a very high post shock density ($\sim 10^8$ cm^{-3}), allowing it to cool in just 10^{-3} yr (comparable to the sound crossing time for the cold bow shock). This shock will be modeled very approximately as isothermal. Interior to this isothermal shock is the free streaming stellar wind.

In the context of this model, there are clearly several locations from which observed ionized emission lines might arise: (1) the high-density, interior, cold bow shock; (2) the stellar mass-loss envelope below the bow shock; and (3) the outer, hot bow shock. The latter is not a significant source given the very high temperatures (and hence low recombination rate) and its relatively small emission measure ($n^2 L$). To evaluate the expected emissivities from the mass-loss envelope and the cold bow shock, we develop a detailed model for the bow shock structure in Section 3 and the ionization in Section 4.

3. BOW SHOCK MODEL

To model the bow shock region, we make use of the analytic treatment by Dyson (1975) modeling a fast stellar wind ablating an expanding dust globule. Dyson developed two limiting cases: (1) with mixing of the two shocked layers (hot gas and cold gas) and (2) without mixing of the shocked layers, resulting in a full tangential discontinuity between the layers. In the following we use the latter approximation. The 3D velocity of the star relative to the ambient medium is taken from the latest orbit of G2 given by Gillessen et al. (2013) and the ambient medium density and temperature as a function of distance from SgrA* were taken from Equation (2) and all are shown in Figure 1.

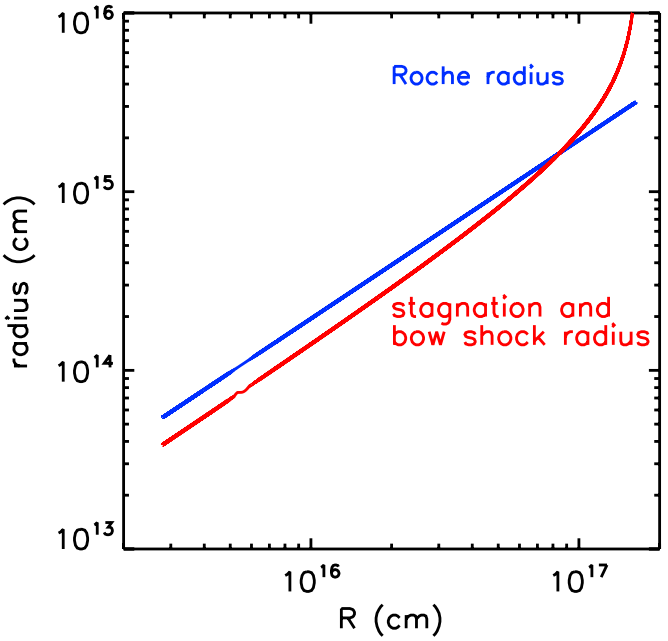

Figure 2. Stagnation radius in front of the star (Equation (8)) and the Roche radius for tidal stripping are shown as a function of distance from SgrA*. The Roche radius was calculated assuming a star mass of 2 $M_\odot$. Inside a 10^{17} cm radius from SgrA*, the emission region is stable against tidal disruption, although tides will shear the tail out behind the star.

(A color version of this figure is available in the online journal.)

Inside a $\sim 5 \times 10^{16}$ cm distance from SgrA*, the mass-loss star is plunging supersonically toward SgrA*. At these radii the star is essentially in free fall, whereas the hot gas is assumed to be in hydrostatic equilibrium (hence having thermal sound speed similar to the circular velocity). The supersonic motion of the star through the hot gas will result in the two bow shocks mentioned earlier: the cold bow shock in the stellar wind material just inside the stagnation radius (see Figure 2), and the hot bow shock in the hot ambient medium just outside the stagnation radius. Figure 3 shows these shocks and the stellar envelope structure as computed for a distance of 10^{16} cm from SgrA* when the star is moving at 3300 km s^{-1} through the ambient medium of density ~ 440 cm^{-3}. The cold bow shock has a thickness of only $\sim 3 \times 10^{12}$ at this point and so it is hardly visible in Figure 3 but its density is 10^8 cm^{-3}, so its potential emission measure ($n^2 L$) is large. We say "potential" since it is also required that the gas be ionized if it is to account for the observed line emission.

The structure and physical conditions in the shocked envelope were computed over the full stellar orbit assuming stellar wind parameters of $V_{\mathrm{wind}} = 100$ km s^{-1}, $\dot{M} = 4 \times 10^{-8}\ M_\odot$ yr^{-1}. Figures 4 and 5 show the derived densities and thicknesses (perpendicular to the bow shock) for the two shocks as a function of the distance from SgrA*. Over most of the orbit the cold shock density is four orders of magnitude higher than that of the hot shock, while the thickness of the hot shock is only ~ 20 times that of the cold shock. It is therefore clear that the cold shock will have a much greater emission measure (EM $\propto n^2 vol$), provided the gas is ionized. Figure 6 shows the tangential flow velocities in the cold and hot show regions. (These velocities are parallel to the bow shock.)

The gas in the hot shock layer flows around the cold shock layer tangentially at velocities ~ 1000 km s^{-1}. The mass-flux of hot shock material intercepting the cold shock provides an

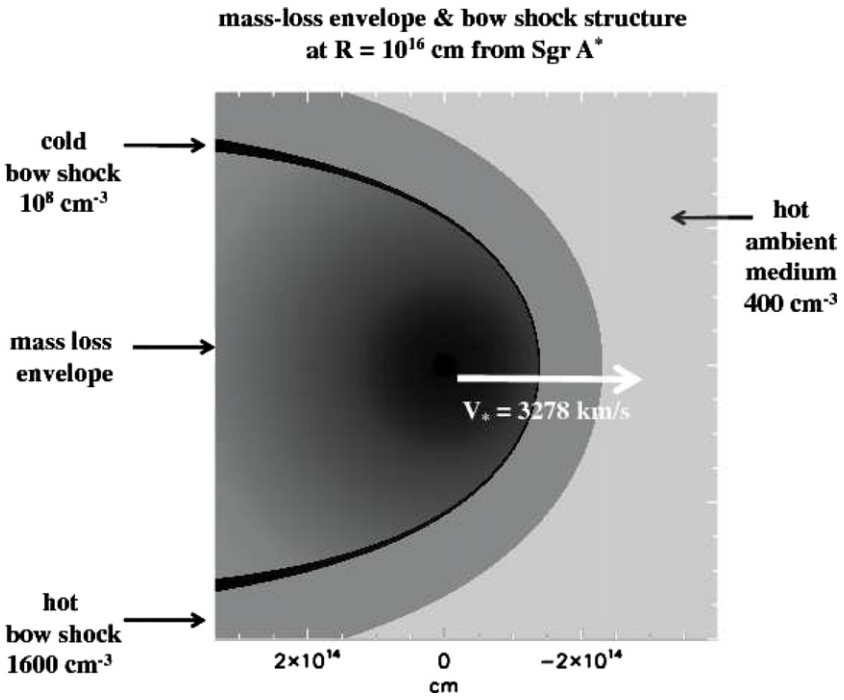

Figure 3. Computed density structure of the mass-loss envelope and bow shocks are shown when the star is 10^{16} cm from Sgr A*. The density is shown with logarithmic scaling from $n = 100$ to 10^{10} cm^{-3} in gray scale. The stellar velocity at this radius is 3278 km s^{-1} and the ambient medium density of the X-ray emitting gas is 400 cm^{-3}. Two bow shocks are formed—a thick one in the shocked hot upstream medium and a very thin, high-density cold layer in the shocked stellar wind. For this model, $V_{\rm wind} = 100\,{\rm km\,s^{-1}}$ and $\dot{M} = 4 \times 10^{-8}\,M_\odot\ {\rm yr}^{-1}$.

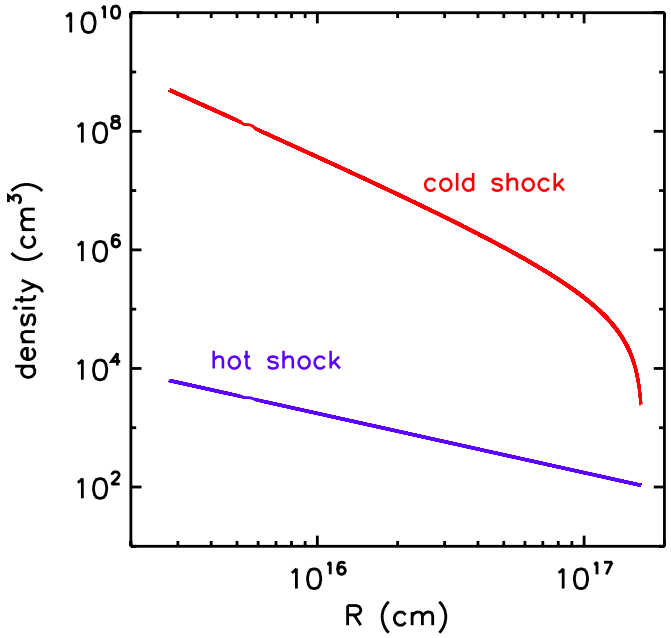

Figure 4. Density of the cold and hot bow shocks are shown as a function of distance from SgrA*. (The density in the cold shock is independent of V_W and $\dot{M}$.)

(A color version of this figure is available in the online journal.)

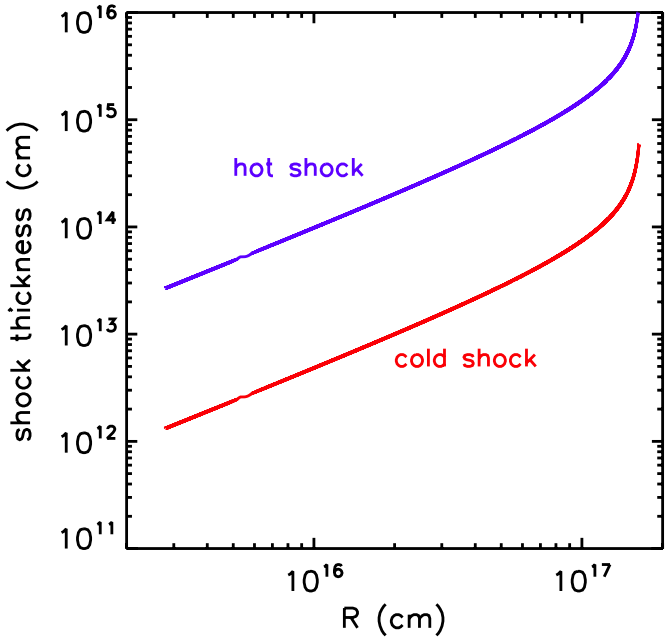

Figure 5. Thickness of the cold and hot bow shocks are shown as a function of distance from SgrA*. (The shock thickness for the cold bow shock scales approximately as $V_W^{-1.5}\dot{M}^{0.5}$ and as $V_W^{1/2}\dot{M}^{1/2}$ for the hot shock.)

(A color version of this figure is available in the online journal.)

upper limit to the cold shock ablation rate. For hot gas densities of $\sim 10^3$ cm^{-3} and an effective radius of 10^{14} cm for the cold shock, this yields a maximum ablation rate of $10^{-10}\,M_\odot$ yr^{-1} which is two orders of magnitude less than the wind mass-loss rate. Ablation is therefore probably not significant.

The derived emission measures (EM) for the cold shock and the mass-loss envelope integrated down to the launch radius ($\sim$0.18 AU for $V_{\rm wind} = 100\,{\rm km\,s^{-1}}$) are shown in Figure 7 as a function of distance from SgrA*. For the bow shock, the EM was calculated only out to radius $\sim 4 \times 10^{15}$, i.e., the area shown in Figure 3. This clearly is a lower limit since there will be significant additional EM in the extended downstream tail of the bow shock. The EM values at $\sim 10^{16}$ cm (or 0.″1) from SgrA* are in reasonable agreement with the Gillessen et al. (2012) value

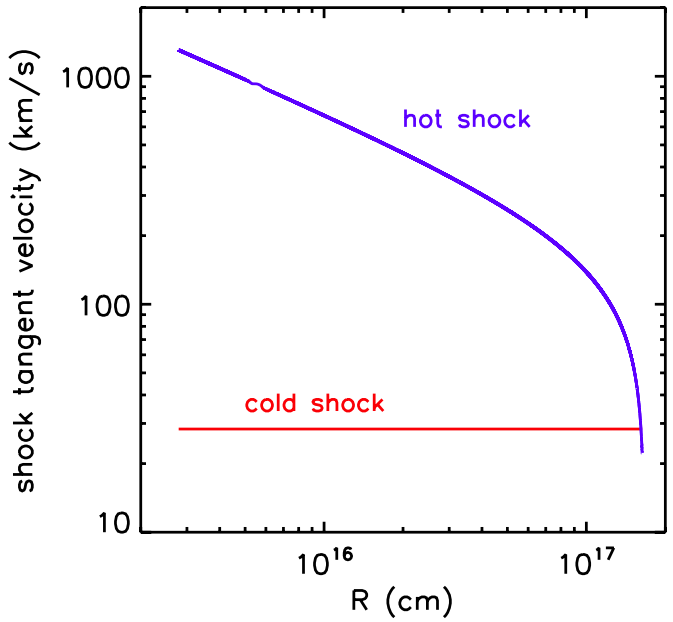

Figure 6. Tangential velocities in the cold and hot bow shocks are shown as a function of distance from SgrA*. (The cold shock tangent velocity will scale linearly with V_W and is independent of $\dot{M}$. The velocity in the hot shock is independent of both parameters.)

(A color version of this figure is available in the online journal.)

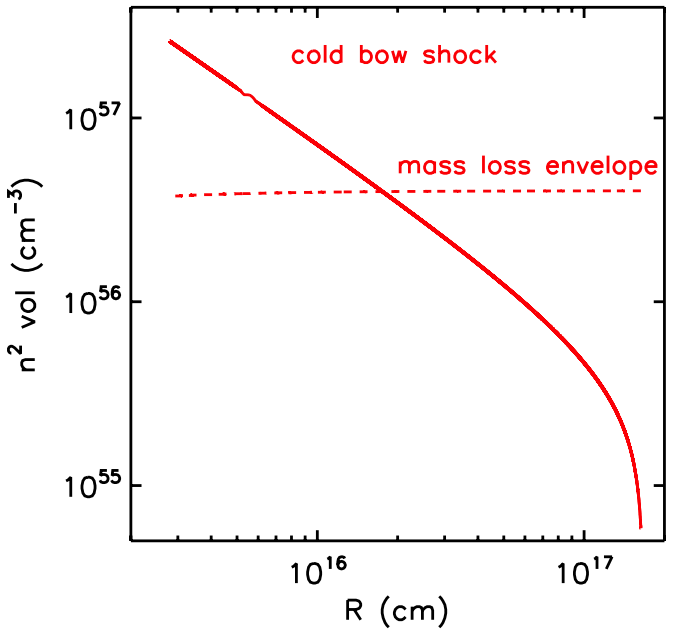

Figure 7. Integrated emission measure ($n^2 vol$) is shown for the cold bow shock and the stellar envelope as a function of distance from Sgr A*. For the mass-loss envelope $n^2 vol$ is constant with a value determined by the adopted mass loss, and very importantly, by the inner radius adopted for the outflow (see discussion following Equation (2)). At distance 10^{16} cm from Sgr A* in mid 2012, the total emission measure for the ionized gas is $\sim 10^{57}$ cm^{-3}. (The emission measure from the cold shock scales as $V_W^{-1/2}\dot{M}^{3/2}$).

(A color version of this figure is available in the online journal.)

of $\sim 10^{57}$ cm^{-3} for the ionized gas, considering that we have not included the downstream tail. The EM of the bow shock is also $\sim$4 times that from the mass-loss envelope. The predicted EM of the bow shock will obviously increase if the mass-loss rate is raised above the adopted $4 \times 10^{-8}\, M_\odot$ yr^{-1}. In the foregoing discussion we have ignored the issue of whether the gas in the three zones will actually be ionized and clearly that is a critical consideration.

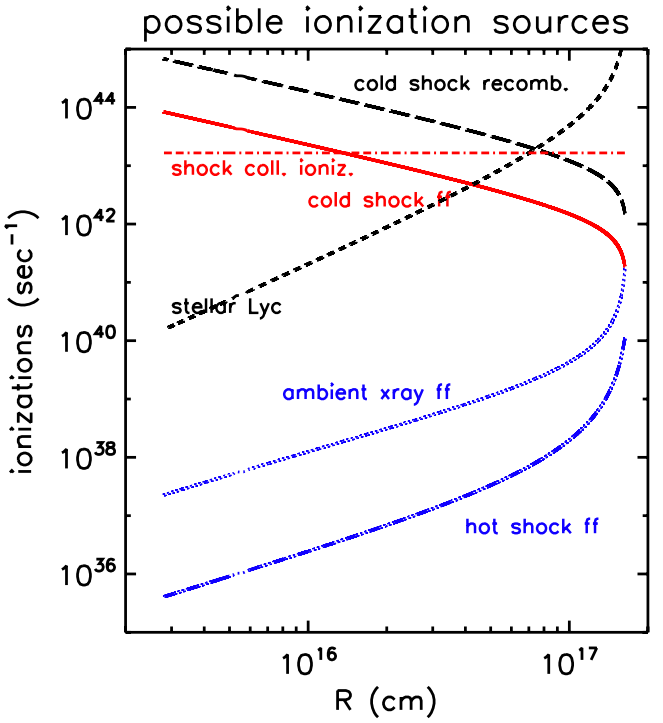

Figure 8. Black dashed line shows the maximum hydrogen recombination rate (to $n > 1$) for the cold bow shock ($=n_e^2 vol\alpha_B$, i.e., assuming complete ionization of the shell) as a function of distance from SgrA*, together with curves showing the possible sources of ionization: collisional ionization of stellar wind material at the bow shock; free–free photons at energy greater than 13.6 eV from the hot X-ray emitting ambient medium, and from the hot and cold bow shock layers; and Lyman continuum photons from hot stars in the inner parsec.

(A color version of this figure is available in the online journal.)

4. IONIZATION

Ionization of the material may potentially be provided by: UV photons from hot stars in the central few parsecs, UV/X-ray photons from the hot plasma in the central parsec or the hot gas (10^5–10^6 and 10^8–10^9 K) in the two bow shocks, or collisions at the inner bow shock where the envelope material moving at 100–500 km s^{-1} is shocked. In the case of photoionization by extended UV sources such as hot stars and X-ray emitting plasma, it is important to recognize that it is not simply a matter of counting photons; one must also estimate the flux into the emission region. If the region of high EM is compact, only a small fraction of the available photons will actually be intercepted.

In Figure 8 we show the $n > 1$ (case B) H I recombination rate for the cold bow shock material together with estimates for the possible ionization rates within the bow shock due to stellar Lyman continuum, free–free emission at greater than 13.6 eV from the hot plasma regions (the two bow shocks and the X-ray emitting ambient medium around SgrA*), and collisional ionization due to mass-loss material passing through the bow shock. In the case of cooling radiation from the hot plasma regions we have included only the free–free continuum, not the line cooling which dominates by a factor of a few at 10^5–10^6 K, and for which some of the photons can ionize H (Shull & McKee 1979). Although these ionization estimates are quite approximate, it is clear that the only viable sources are

the collisional ionization at the bow shock and the gas cooling within the "cold" bow shock where $T \sim 10^5$–10^6 K.

The Lyman continuum from the young stars in the galactic nucleus is not well constrained but we adopted the equivalent of an O5 star within the central 1 pc radius, i.e., a Lyman continuum production rate of $Q = 10^{50}$ Lyc s^{-1}. This production rate implies an average photon flux of $\sim 3 \times 10^{12}$ Lyc cm^{-2} s^{-1} and integrating over the bow shock area we arrive at the estimate given in Figure 8. Although the production rate of Lyman continuum photons from hot stars is large, the area of the bow shock is small, so very few of them will be intercepted. Similarly, although there is a potentially large EM at the base of the mass-loss envelope, the intercepted area of that region at radius 0.18 AU is so small that the material would not be ionized, except by UV from the stellar accretion shock. The latter may of course be substantial since the T Tauri star winds exhibit ionized gas emission lines and some of the gas arriving at the bow shock may already be ionized.

4.1. Constancy of the Emission Line Fluxes

Gillessen et al. (2013) report that the observed line fluxes for the Brγ emission are constant to within 10% over the four year period 2008 May to 2012 May. This is very surprising, given the fact that its distance from SgrA* changed from 3.6 to 1.3×10^{16} cm and its 3D velocity increased from 1500 to 2900 km s^{-1}. In almost any model, one would expect the gas mass and/or the excitation of the emission in G2 to correlate with the distance from SgrA* and/or infall velocity. In the context of the model proposed here, the approximate constancy of the flux might be understood if the dominant source of ionization is collisional, as stellar wind material from the inside passes through the cold bow shock at 100–500 km s^{-1}. In this case, the total number of ionizations per second (hence the line emission flux) will be constant and simply a few times the number of atoms passing through the shock front. This number flux is $\sim 1.6 \times 10^{42}$ s^{-1} for $\dot{M} = 4 \times 10^{-8}\, M_\odot$ yr^{-1}. Since the H I ionization energy of 13.6 eV corresponds to an H I particle velocity of 50 km s^{-1}, this estimate should be multiplied by a factor $\sim (V_w/50 \text{ km s}^{-1})^2$ to account for the energy available in the shock compared to what is needed to ionize H I. In Figure 8, we have taken this factor to be $\sim$10 for the collisional ionization rate estimate. Combining this collisional ionization with the photoionization from free–free photons at >13.6 eV yields an ionization rate $\sim 10^{44}$ s^{-1}, similar to what is needed to maintain the observed emission. If the ionization is not due to collisions at the bow shock, it is unclear how to explain the constancy of the emission line fluxes since all the other sources of ionization vary with distance from SgrA*.

It is worthwhile to note that some variation in the emission line fluxes is a desirable feature of any model in which G2 comes in from larger radii. If the fluxes are relatively constant with radius, one should expect to see a large number of similar emission regions at the larger radii—so far these have not been seen. A drop off in the expected emissivity out beyond several 10^{16} cm (as shown in Figure 7) is therefore a desirable feature, in that it reduces the visibility of such precursors.

5. THE STAR AND ITS ORBIT

Eckart et al. (2013) report detection of an object they call DSO in the K- and L-band continua with position and proper motion similar to G2. The source has a very low color temperature, $\sim$500 K, and the K-band magnitude is $\sim$18.9 mag. For 1–2 $M_\odot$ T Tauri stars, $M_K \sim$ 2–4 mag (Baraffe et al. 1998; L. A. Hillenbrand 2013, private communication). At the Galactic center, the unextincted apparent magnitude will be 16.5–18.5 mag in the K-band. The K-band extinction toward the Galactic center will dim it a further $\sim$3 mag, implying $m_K \sim$ 20 mag. Thus, the star itself, if it is a T Tauri star, would be very difficult to directly detect unless it is in a period of enhanced activity. In fact, Eckart et al. (2013) have suggested that G2/DSO is a dust enshrouded star. One would also expect there to be mass-loss red giant stars in the galactic nucleus; however, such stars can probably be ruled out for G2 since their brightness would be higher than the observed L-band flux.

The origin of the high eccentricity orbit of G2 remains poorly understood. Although one might posit stellar interactions in a triplet system, these would generally be disruptive of any circumstellar material. The injection to a highly eccentric orbit from circular orbit requires a velocity kick of $\sim$500 km s^{-1}. To provide such an impulse with a single star–star scattering would require a close approach well inside 1 AU. Such close encounters would certainly disrupt any large protoplanetary disk such as that invoked by Murray-Clay & Loeb (2012)—and possibly also the inner disk from which the T Tauri star winds are launched (as discussed here).

In the face of such difficulties, it is attractive to consider the possibility that the young stars would have to be formed in eccentric orbits through collisions of gas clumps with cancellation of angular momentum (C. Alig et al. 2013, in preparation). The gas motions in the mini-spiral inside 1 pc have substantial non-circular velocities and the molecular ring or CND at 1–3 pc radius is inclined at 50° –75° to the Galactic plane (Jackson et al. 1993; Christopher et al. 2005)—both of which indicate substantial non-planar, non-circular dynamics for the ISM there.

Alternatively, the increase in eccentricity might be built up by a series of many smaller amplitude scatterings (e.g., Murray-Clay & Loeb 2012). Is it possible that a large increase in the eccentricity from an initial circular orbit could be induced similar to the Kozai oscillations in exoplanetary systems? If the star was formed in the young stellar ring at 2×10^{17} cm radius, the orbital period is $\sim$200 yr. The star and any companions could have then orbited the galactic center $\sim 10^4$ times. Mass clumps associated with both the circumnuclear gas disk and stars might possibly provide perturbations to initiate the process.

6. IMPLICATIONS

The usually assumed mass for G2 of 3 $M_\oplus$ was derived by Gillessen et al. (2012) assuming the gas is distributed homogeneously with density $\sim 6 \times 10^5$ cm^{-3}. For our model the emission measure is produced by gas at density $\sim 10^8$ cm^{-3}, resulting in a decrease in the required mass of emitting gas by a factor 200.

It would be a shame if this object, which so intrigues us now, were to disappear this September at pericenter. The model proposed here looks to a brighter future. At pericenter, the tidal radius is reduced to $\sim$1–3 AU—this major disruption in the mid-radii of the disk will result in stripping to the exterior and some deposition to the interior disk—inside 1 AU. The latter could result in greatly enhanced stellar mass-loss rates—hence much brighter emission at and after pericenter passage for several years.

We would like to thank Lynne Hillenbrand for helpful discussions on the properties of TTauri stars and Andreas Eckart for suggestions. AB thanks Caltech for the hospitality of a

visit which stimulated this project. We acknowledge discussions with Alessandro Ballone and Marc Schartmann who are further developing this model with detailed numerical simulation.

REFERENCES

Baganoff, F. K., Maeda, Y., Morris, M., et al. 2003, ApJ, 591, 891
Baraffe, I., Chabrier, G., Allard, F., & Hauschildt, P. H. 1998, A&A, 337, 403
Blandford, R. D., & Payne, D. G. 1982, MNRAS, 199, 883
Burkert, A., Schartmann, M., Alig, C., et al. 2012, ApJ, 750, 58
Christopher, M. H., Scoville, N. Z., Stolovy, S. R., & Yun, M. S. 2005, ApJ, 622, 346
Dyson, J. E. 1975, Ap&SS, 35, 299
Eckart, A., Mužić, K., Yazici, S., et al. 2013, A&A, 551, A18
Gillessen, S., Genzel, R., Fritz, T. K., et al. 2012, Natur, 481, 51
Gillessen, S., Genzel, R., Fritz, T. K., et al. 2013, ApJ, 763, 78
Hartigan, P., Edwards, S., & Ghandour, L. 1995, ApJ, 452, 736
Jackson, J. M., Geis, N., Genzel, R., et al. 1993, ApJ, 402, 173
McKee, C. F., & Hollenbach, D. J. 1980, ARA&A, 18, 219
Meyer, F., & Meyer-Hofmeister, E. 2012, A&A, 546, L2
Muno, M. P., Baganoff, F. K., Bautz, M. W., et al. 2004, ApJ, 613, 326
Murray-Clay, R. A., & Loeb, A. 2011, arXiv:1112.4822
Sazonov, S., Sunyaev, R., & Revnivtsev, M. 2012, MNRAS, 420, 388
Shcherbakov, R. V., & Baganoff, F. K. 2010, ApJ, 716, 504
Shull, J. M., & McKee, C. F. 1979, ApJ, 227, 131
White, R. J., & Hillenbrand, L. A. 2004, ApJ, 616, 998
Yuan, F., Quataert, E., & Narayan, R. 2003, ApJ, 598, 301